

Identifying the human optic radiation using diffusion imaging and fiber tractography

Anthony J. Sherbondy

Department of Electrical Engineering, Stanford University,
Stanford, CA, USA



AQ1

Robert F. Dougherty

Department of Psychology, Stanford University,
Stanford, CA, USA



AQ1

Sandy Napel

Department of Radiology, Stanford University,
Stanford, CA, USA



AQ1

Brian A. Wandell

Department of Psychology, Stanford University,
Stanford, CA, USA



AQ1

Measuring the properties of the white matter pathways from retina to cortex in the living human brain will have many uses for understanding visual performance and guiding clinical treatment. For example, identifying the Meyer's loop portion of the optic radiation (OR) has clinical significance because of the large number of temporal lobe resections. We use diffusion tensor imaging and fiber tractography (DTI-FT) to identify the most likely pathway between the lateral geniculate nucleus (LGN) and the calcarine sulcus in sixteen hemispheres of eight healthy volunteers. Quantitative population comparisons between DTI-FT estimates and published postmortem dissections match with a spatial precision of about 1 mm. The OR can be divided into three bundles that are segmented based on the direction of the fibers as they leave the LGN: Meyer's loop, central, and direct. The longitudinal and radial diffusivities of the three bundles do not differ within the measurement noise; there is a small difference in the radial diffusivity between the right and left hemispheres. We find that the anterior tip of Meyer's loop is 28 ± 3 mm posterior to the temporal pole, and the population range is 1 cm. Hence, it is important to identify the location of this bundle in individual subjects or patients.

Keywords: diffusion imaging, fiber tractography, lateral geniculate nucleus, optic radiation

Citation: Sherbondy, A. J., Dougherty, R. F., Napel, S., & Wandell, B. A. (2008). Identifying the human optic radiation using diffusion imaging and fiber tractography. *Journal of Vision*, 0(0):1, 1–10, <http://journalofvision.org/0/0/1/>, doi:10.1167/0.0.1.

Introduction

In the early 19th century Louis-Pierre Gratiolet used brain fixation and dissection to identify and describe the optic radiation (OR) (Leuret & Gratiolet, 1839). This important work showed that retinal signals were sent to localized regions of cortex. This measurement supported the theory of functional specialization of sensory processing in the brain, contradicting the popular belief at the time that the cerebrum was equipotent (Schmahmann & Pandya, 2006).

The OR remains an important subject matter for neuro-anatomical inquiry. Measuring the properties of the white matter pathways from retina to cortex in the living human brain will have many uses for understanding visual performance and disabilities. In addition, there has been a great deal of interest in documenting the specific path followed by the OR as it emerges from the lateral geniculate nucleus (LGN) and heads to the calcarine fissure in posterior cortex. The interest is due to widely used neurosurgical interventions that involve resection of

the anterior temporal lobe (Yasargil, Ture, & Yasargil, 2004). Anterior temporal lobe resections are performed for several reasons, including tumors and lesions (Choi, Rubino, Fernandez-Miranda, Abe, & Rhoton, 2006; Peltier, Travers, Destrieux, & Velut, 2006), arteriovenous malformations (Kikuta et al., 2006; Okada et al., 2007), and epileptic foci (Choi et al., 2006; Ebeling & Reulen, 1988; Krolak-Salmon et al., 2000; Peltier et al., 2006; Powell et al., 2005; Rubino, Rhoton, Tong, & Oliveira, 2005; Sincoff, Tan, & Abdulrauf, 2004; Taoka et al., 2005; Yasargil et al., 2004). A portion of the OR emerges from the LGN and passes into the anterior temporal lobe before looping back to posterior cortex (Figure 1). This region of the OR, called Meyer's loop (Meyer, 1907), carries signals that represent the entire contralateral upper visual field; avoiding damage to Meyer's loop is essential for preserving this portion of the patient's visual field.

The location of Meyer's loop is variable, with its anterior position varying as much as 1 cm between individuals (Ebeling & Reulen, 1988). Thus, identifying its location in individual patients is of significant value in pre-surgical planning. Currently, DTI-FT offers the only

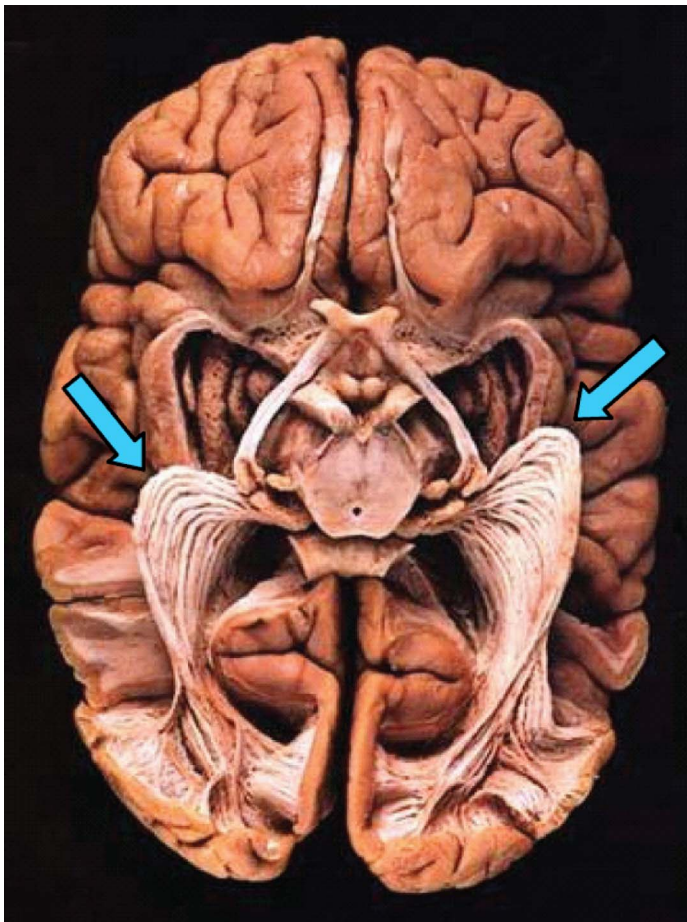


Figure 1. The optic radiation exposed (virtual hospital). A brain, viewed from below, is prepared using Klingler's fiber dissection technique. Meyer's loop, the anterior extension into the temporal lobe, is indicated by the arrows.

78 non-invasive method for measuring the course of white
 79 matter tracts in vivo. The identification of the OR, and in
 80 particular the Meyer's loop portion, has received a
 81 significant amount of attention from the DTI-FT com-
 82 munity (Behrens, Johansen-Berg et al., 2003; Catani,
 83 Jones, Donato, & Ffytche, 2003; Ciccarelli et al., 2005;
 84 Conturo et al., 1999; Kikuta et al., 2006; Okada et al.,
 85 2007; Powell et al., 2005; Taoka et al., 2005; Yamamoto,
 86 Yamada, Nishimura, & Kinoshita, 2005). Despite some
 87 success, DTI-FT estimates have difficulty identifying the
 88 OR and particularly the Meyer's loop section (Miller,
 89 2005; Powell et al., 2005; Yamamoto et al., 2005).

90 This paper uses the ConTrack algorithm (Sherbondy,
 91 Dougherty, Ben-Shachar, Napel, & Wandell, 2008) to
 92 identify the OR. This algorithm locates key OR landmarks
 93 at positions that match those derived using high-quality
 94 dissection methods (Ebeling & Reulen, 1988). Finally,
 95 using estimates from a healthy population, we document
 96 the longitudinal and radial diffusion characteristics along
 97 the entire course of the optic radiation.

Methods

Subjects

102 Data were obtained from eight healthy subjects with no
 103 history of neurological disease, head injury, or psychiatric
 104 disorder. The Stanford Panel on Human Subjects in
 105 Medical and Non-Medical Research approved all proce-
 106 dures. The eight volunteer subjects (S1: 32y male; S2: 24y
 107 male; S3: 27y male; S4: 24y male; S5: 27y male; S6: 23y
 108 male; S7: 23y female; S8: 35y male) were recruited from
 109 the Stanford University campus. Written informed consent
 110 was obtained from all subjects.

Data acquisition

112 The DTI protocol used 8–10 repetitions of a 90-s whole-
 113 brain scan. The scans were averaged to improve signal
 114 quality. The pulse sequence was a diffusion-weighted
 115 single-shot spin-echo, echo planar imaging sequence
 116 (63 msec TE; 6 s TR; 260 mm FOV; 128×128 matrix
 117 size; ± 110 kHz bandwidth; partial k -space acquisition). We
 118 acquired 48–54 axial, 2-mm-thick slices (no skip) for two
 119 b -values, $b = 0$ and $b = 800$ s/mm². The high b -value was
 120 obtained by applying gradients along 12 different diffu-
 121 sion directions. Two gradient axes were energized
 122 simultaneously to minimize TE and the polarity of the
 123 effective diffusion-weighting gradients was reversed for
 124 odd repetitions to reduce cross-terms between diffusion
 125 gradients and both imaging and background gradients.
 126 While Jones (2004) suggests that measuring more diffu-
 127 sion directions might be a more efficient way to reliably
 128 estimate diffusion tensors of arbitrary orientation, our
 129 signal-to-noise ratio is sufficiently high from our 8–10
 130 repeats to produce very reliable tensor estimates. We have
 131 confirmed this in a subset of subjects by comparing
 132 bootstrapped tensor uncertainty estimates from 60-direction
 133 data with the 12-direction data reported here. With our high
 134 SNR, tensor uncertainty is limited by physiological noise
 135 rather than measurement noise.

136 We also collected high-resolution T1-weighted anatom-
 137 ical images for each subject using an 8-minute sagittal
 138 3D-SPGR sequence ($1 \times 1 \times 1$ mm voxel size). The
 139 following anatomical landmarks were manually defined in
 140 the T1 images: the anterior commissure (AC), the
 141 posterior commissure (PC), and the mid-sagittal plane.
 142 With these landmarks, we used a rigid-body transform
 143 to convert the T1-weighted images to the conventional
 144 AC–PC aligned space.

Data preprocessing

147 Eddy current distortions and subject motion in the
 148 diffusion-weighted images were removed by a 14-parameter
 149

99
100

101

102

103

104

105

106

107

108

109

110

111

112

113

114

115

116

117

118

119

120

121

122

123

124

125

126

127

128

129

130

131

132

133

134

135

136

137

138

139

140

141

142

143

144

145

146

147

148

149

150 constrained non-linear co-registration based on the expected
 151 pattern of eddy-current distortions given the phase-encode
 152 direction of the acquired data (Rohde, Barnett, Basser,
 153 Marengo, & Pierpaoli, 2004).

154 Each diffusion-weighted image was registered to the
 155 mean of the (motion-corrected) non-diffusion-weighted
 156 ($b = 0$) images using a two-stage coarse-to-fine approach
 157 that maximized the normalized mutual information. The
 158 mean of the non-diffusion-weighted images was automati-
 159 cally aligned to the T1 image using a rigid body mutual
 160 information algorithm. All raw images from the diffusion
 161 sequence were resampled to 2-mm isotropic voxels by
 162 combining the motion correction, eddy-current correction,
 163 and anatomical alignment transforms into one omnibus
 164 transform and resampling the data using a 7th-order
 165 b-spline algorithm based on code from SPM5 (Friston
 166 & Ashburner, 2004).

167 An eddy-current intensity correction (Rohde et al.,
 168 2004) was applied to the diffusion-weighted images at
 169 the resampling stage. We note that the 7th-order b-spline
 170 interpolation does not require image variance correction
 171 (Rohde, Barnett, Basser, & Pierpaoli, 2005) due to the
 172 large support kernel. Preserving the signal variance
 173 structure in the interpolated data is crucial for an accurate
 174 bootstrap variance estimate.

175 The rotation component of the omnibus coordinate
 176 transform was applied to the diffusion-weighting gradient
 177 directions to preserve their orientation with respect to the
 178 resampled diffusion images. The tensors were then fit
 179 using a least-squares algorithm. We confirmed that the
 180 DTI and T1 images were aligned to within a few
 181 millimeters near the optic radiation. This confirmation
 182 was done by manual inspection by one of the authors
 183 (RFD). In regions prone to susceptibility artifacts, such as
 184 orbito-frontal and inferior temporal regions, the mis-
 185 alignment was somewhat larger due to uncorrected EPI
 186 distortions.

187 All the custom image processing software is available
 188 as part of our open-source mrDiffusion package available
 190 for download from <http://vistalab.stanford.edu/software>.

Identification of OR with ConTrack

191

192 The ConTrack algorithm can find white matter path-
 193 ways such as the OR that are known to exist but are
 194 difficult for other algorithms to detect (Sherbondy et al.,
 195 2008). Similar to other modern probabilistic DTI-FT
 196 algorithms, ConTrack can find pathways that are difficult
 197 for deterministic DTI-FT techniques because it allows
 198 many more possible local pathway orientations for each
 199 DTI sample point.

200 ConTrack improves upon other probabilistic DTI-FT
 201 algorithms by separating pathway sampling from pathway
 202 scoring and ranking. Specifically, one component of
 203 ConTrack, pathway sampling, is designed to search the set
 204 of all possible pathways connecting two regions within the
 205 DTI data (Figure 2). Another component of ConTrack,
 206 pathway scoring, is designed to score the sampled pathways
 207 with a function that evaluates the anatomical validity of the
 208 pathway by incorporating its fit to the DTI data as well as
 209 prior knowledge. Finally, the user sets the lower score
 210 threshold for selecting a subset of pathways that estimate
 211 the white matter anatomy of interest. This subset can then
 212 be used for inferring properties about the connection
 213 between the two brain regions. By separating sampling
 214 and scoring procedures, the validity of each potential white
 215 matter pathway is considered independently.

216 In the case of the pathways of the OR, previous
 217 probabilistic approaches allow the high probability direct
 218 connections to mask the presence of the slightly lower
 219 probability curved pathways comprising Meyer's loop.
 220 This competition reduces the likelihood of observing
 221 Meyer's loop (Behrens, Johansen-Berg, et al., 2003;
 222 Jbabdi, Woolrich, Andersson, & Behrens, 2007) and
 223 makes the loop difficult to discriminate from spurious
 224 pathways that are not within the OR (Powell et al., 2005).
 225 The independent assignment of validity scores to every
 226 pathway connecting the lateral geniculate nucleus (LGN)
 227 region of interest (ROI) and the calcarine sulcus ROI
 228 allows ConTrack to find the Meyer's loop as well as the
 229 higher scoring direct pathways of the OR.

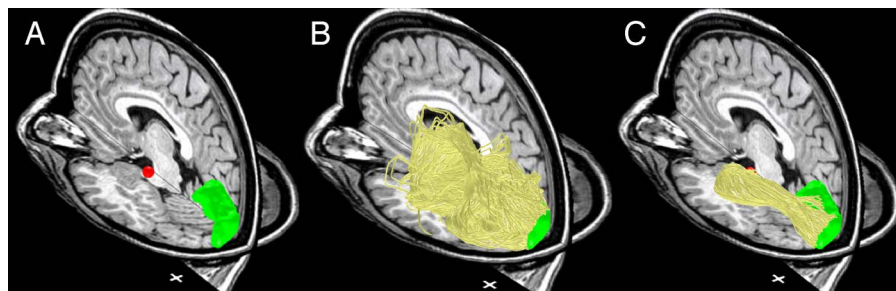


Figure 2. Overview of the ConTrack method for identifying the optic radiation. Co-registered T1 and estimated fiber tracts are shown. (A) LGN (red) and calcarine sulcus (green) ROIs identified by manual segmentation. (B) A large set of potential pathways (yellow) connecting the two ROIs are generated using ConTrack. (C) The top scoring subset is chosen based on a user chosen threshold (Table 1). Cross hairs: 1 × 1 cm (Subject S1).

230 The ConTrack DTI-FT method is comprised of the
 231 following three stages: ROI specification, pathway sam-
 232 pling, and pathway scoring and selection.

233

234 ROI specification

235 The LGN ROI was identified within the DTI data. First,
 236 the optic chiasm was located from a fractional anisotropy
 237 (FA) map. From this location, one can automatically
 238 follow the optic tract from the chiasm to the LGN with a
 239 streamlines tracing technique (STT) (Basser, Pajevic,
 240 Pierpaoli, Duda, & Aldroubi, 2000; Conturo et al., 1999;
 241 Mori, Crain, Chacko, & van Zijl, 1999). We placed a
 242 4-mm radius sphere to cover the STT tracts that reached
 243 the most posterior and lateral portion of the thalamus. The
 244 size of this ROI (270 mm³) was chosen to include the
 245 entirety of the LGN, which ranges from 91 to 157 mm³
 246 (Andrews, Halpern, & Purves, 1997). The second ROI
 247 was chosen to cover the calcarine sulcus of the occipital
 248 lobe. This ROI was manually segmented in each hemi-
 249 sphere from the mean non-diffusion-weighted images
 250 using itkSnap (Yushkevich et al., 2006). The higher-
 251 resolution T1 images were used to resolve occasional
 252 ambiguities in the lower-resolution DTI images.

253

254 Pathway sampling

255 ConTrack's pathway sampling algorithm uses both ROIs
 256 as boundaries defining potential starting points and
 257 retained only pathways that satisfied the following criteria:
 258 pathway length was <300 mm, pathway bending angle for
 259 a single step could not exceed 130°, pathways could not
 260 step through manually defined regions of gray matter, and
 261 pathways had an endpoint within both ROIs. The algo-
 262 rithm was run to collect 100,000 pathway samples between
 263 the two ROIs and the pathway step size was set to 1 mm.
 264 This required between 50 and 120 minutes of execution

time per hemisphere on a single 1 GHz AMD Opteron core
 with 2 GB of RAM.

265

266

267

Pathway scoring and selection

268

269 Many of the 100,000 sampled pathways will be a poor
 270 representation of the optic radiation anatomy. The path-
 271 ways are ordered by a score (Q) that assesses their
 272 anatomical validity, where highest scoring is most likely
 273 valid. The scoring function combines the pathway fit to
 274 the DTI data with prior information on tract smoothness
 275 and length. Specifically, the score is divided into two
 276 terms. One term evaluates the likelihood of observing the
 277 data given the pathway. The second term evaluates the
 278 likelihood of the pathway, itself.

279 To run the scoring algorithm the user must decide on
 280 the values of three key parameters. One parameter, η ,
 281 influences the penalty for a mismatch between the local
 282 pathway direction and the principal diffusion direction.
 283 This parameter was set to its default value, 0.175. A
 284 second parameter, σ_c , influences the penalty for local
 285 pathway curvature (Sherbondy et al., 2008). This param-
 286 eter was set to 14°. The third parameter, λ , influences the
 287 preferred pathway length. Because there is considerable
 288 range in the length of optic radiation pathways, we set
 289 this parameter to a value that does not discriminate
 290 between long and short pathways, $\lambda = 1$. The score is the
 291 product of local scores for many unit step intervals along
 292 a pathway. Again, to avoid a length penalty, we used the
 293 geometric mean of these products. More details on
 294 ConTrack are provided elsewhere (Sherbondy et al.,
 295 2008).

296 The subset of pathways representing the optic radiation
 297 was selected by eliminating pathways with a score below
 298 a threshold score (Q_t) that was manually determined for
 299 each hemisphere using DTI-Query (Sherbondy, Akers,
 300 Mackenzie, Dougherty, & Wandell, 2005). The Q_t value
 301 was first set as the highest score of any pathway. Then, Q_t
 302 was lowered until three distinct bundles of the OR were

269

270

271

272

273

274

275

276

277

278

279

280

281

282

283

284

285

286

287

288

289

290

291

292

293

294

295

296

297

298

299

300

301

302

t1.2		Threshold (Q_t)		No. of pathways > threshold		Pruned pathways	
t1.4	ID	L	R	L	R	L	R
t1.6	S1	0.8	1.2	7352	8016	884 (12%)	44 (0.5%)
t1.8	S2	1.5	1.5	4498	13791	7 (0.1%)	3 (0.02%)
t1.10	S3	1.2	1.5	11924	16779	28 (0.2%)	7 (0.04%)
t1.12	S4	0.5	1.2	2670	5720	642 (24%)	26 (0.4%)
t1.14	S5	0.8	0.5	47134	13217	0 (0%)	298 (2%)
t1.16	S6	1.2	0.7	12918	2714	6 (0.04%)	182 (7%)
t1.18	S7	0.5	1.4	7749	11340	129 (17%)	18 (0.2%)
t1.20	S8	0.8	1.2	2628	4854	480 (18%)	128 (2.6%)

t1.22 Table 1. Summary of the optic radiation selection process. The first column contains the score threshold (Q_t). The second column is the number of pathways (out of 100,000) above this threshold. The third column is the number (percentage) of above-threshold pathways that were manually pruned using the method described in the text.

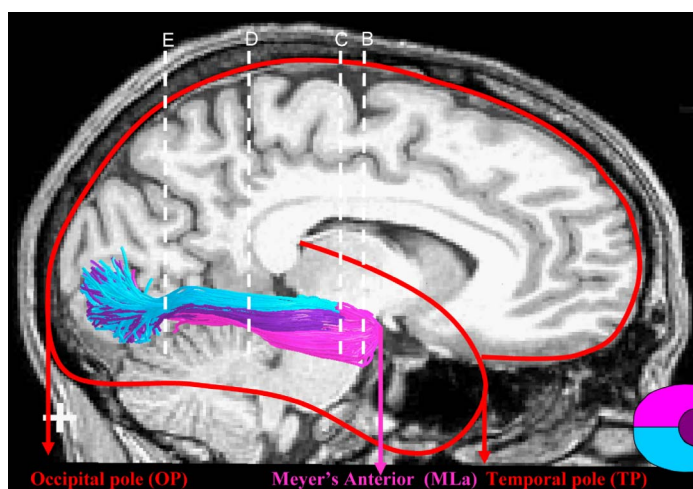


Figure 3. Anatomical coordinates for assessing the optic radiation location, as defined by Ebeling and Reulen (1988). The ConTrack OR estimates are illustrated on the right hemisphere. The background image is a co-registered mid-sagittal T1 image. The red outline of the brain indicates the position of the temporal pole (TP) and the occipital pole (OP). The ConTrack OR estimates are colored according to the direct (blue), central (purple), and Meyer's loop (pink) bundles. These carry information about the lower, foveal, and upper left visual field, respectively (see inset, lower right). The anterior position of Meyer's loop (MLa) is labeled. The white dotted lines (B, C, D, and E) are the locations of the coronal images in Figure 5. Subject S1. Cross hair: 1×1 cm.

visualized and only a few pathways remained that deviated significantly from one of the three bundles. Pathways that intersected more than one voxel of visually obvious regions of gray matter or cerebral spinal fluid also were manually removed. This hand editing is necessary because automatic tissue identification algorithms do not provide adequate accuracy. The percentage of discarded pathways compared to the retained subset of OR pathways was generally small (Table 1).

Identification of anatomical landmarks used to position the OR

In order to compare the OR estimated by ConTrack with the results from dissection studies, we identified the following anatomical landmarks: anterior tip of the temporal pole (TP), anterior tip of Meyer's loop (MLa), anterior tip of the temporal horn (TH), and the posterior tip of the occipital pole (OP) (Figure 3). The TP, TH, and OP positions were all identified in each hemisphere using the non-diffusion-weighted image from the diffusion imaging sequence (see above). The position of MLa was determined as the furthest anterior position of pathways identified as Meyer's loop. The OR pathway estimates were manually separated into three distinct bundles. The Meyer's loop was determined to be any pathway that projected in an orientation inferior and anterior from the

LGN. The central bundle was determined by selecting any pathway that extended in a lateral direction from the LGN. The direct bundle was defined as any remaining pathway that was neither the Meyer's loop nor the central bundle.

The ConTrack software and documentation is available as an open-source distribution from the Web site (<http://www.simtk.org/contract>).

Results

Position and course of the OR

The OR was identified in all hemispheres of the 8 healthy subjects (Figure 4). The most anterior position of

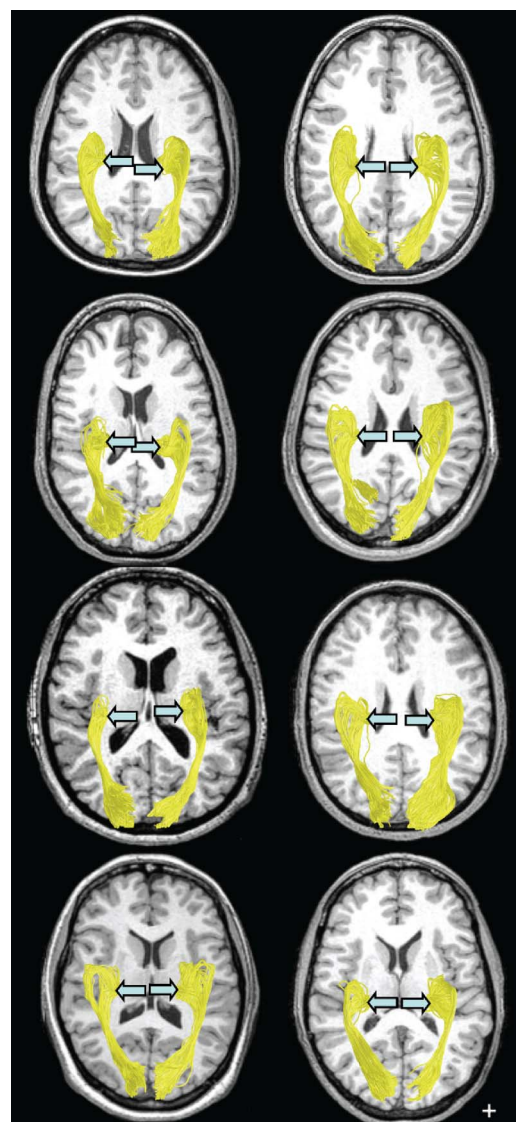


Figure 4. Estimated OR in 16 hemispheres, viewed from below. The position of the LGN (blue arrow) is indicated for each hemisphere. Cross hair: 1×1 cm.

343 the Meyer's loop was found to be an average distance of
 344 28 mm from the temporal pole, in agreement with the
 345 dissection results of Ebeling and Reulen (1988). Further-
 346 more, the measurements of the distance between the
 347 anterior location of the Meyer's loop and the occipital
 348 pole as well as the location of this point of the OR with
 349 respect to the tip of the temporal horn agree quite well
 350 with the dissection results (see Discussion).

351 To verify that our measurements were robust to outliers,
 352 we also measured the most anterior position after exclu-
 353 ding the 5% of fibers in Meyer's loop closest to the
 354 temporal pole. The average position of this measurement
 355 differed from the reported position by only 2 mm.

356 In addition to the distance measurements of the
 357 position of the OR with respect to anatomical landmarks,
 358 we also examined the course of the OR along a sequence
 359 of coronal sections. In Figure 5, one representative
 360 subject (S1) demonstrates the correspondence between
 361 ConTrack's estimation of the OR and the dissected fibers
 362 of Ebeling and Reulen (1988). By visual inspection, the
 363 ordering (topological) relationship between the central,
 364 direct, and Meyer's bundles along the course of the OR
 365 matches the illustrations reproduced from Ebeling and
 366 Reulen.

368 Diffusivity within the OR

369 To characterize the diffusion properties of the OR, we
 370 computed the longitudinal and radial diffusivity values for

371 the separate OR bundles (Meyer's, Central, Direct) and
 372 for all of the white matter (All). Longitudinal diffusivity is
 373 the largest eigenvalue of the diffusion tensor, and radial
 374 diffusivity is the mean of the remaining two eigenvalues.

375 To identify voxels within the core of the optic radiation
 376 and the white matter, we considered only voxels with a
 377 linearity index (C_L) greater than 0.3 (see Figure 6).
 378 Linearity measures anisotropy; it is the positive difference
 379 between the largest two eigenvalues of the diffusion tensor
 380 divided by the sum of its eigenvalues (Peled, Gudbjartsson,
 381 Westin, Kikinis, & Jolesz, 1998). We previously described
 382 how this value may be used to indicate how likely the
 383 DTI signal is a measurement from one fascicle orienta-
 384 tion (Sherbondy et al., 2008). The linearity values select
 385 diffusion data along the pathways that are more likely to
 386 be within the core of the OR and less corrupted by
 387 partial voluming with CSF, gray matter, or crossing fiber
 388 tracts.

389 For each hemisphere, we estimated 4 mean longitudinal
 390 diffusivity values and 4 mean radial diffusivity values
 391 (Meyer's, Central, Direct, All). Mean \pm SE longitudinal
 392 diffusivities (in units of $\mu\text{m}^2/\text{msec}$) were 1.56 ± 0.01 ,
 393 1.57 ± 0.01 , 1.57 ± 0.01 , and 1.49 ± 0.01 for the four
 394 groups, respectively. Mean \pm SE radial diffusivities were
 395 0.448 ± 0.006 , 0.445 ± 0.007 , 0.442 ± 0.008 , and $0.414 \pm$
 396 $0.005 \mu\text{m}^2/\text{msec}$, respectively.

397 The only significant difference between the diffusivity
 398 measures was between the (All) group and each of the OR
 399 groups ($p < 0.01$, two-sample t -test). We also averaged the
 400 three optic radiation bundles and compared the left and

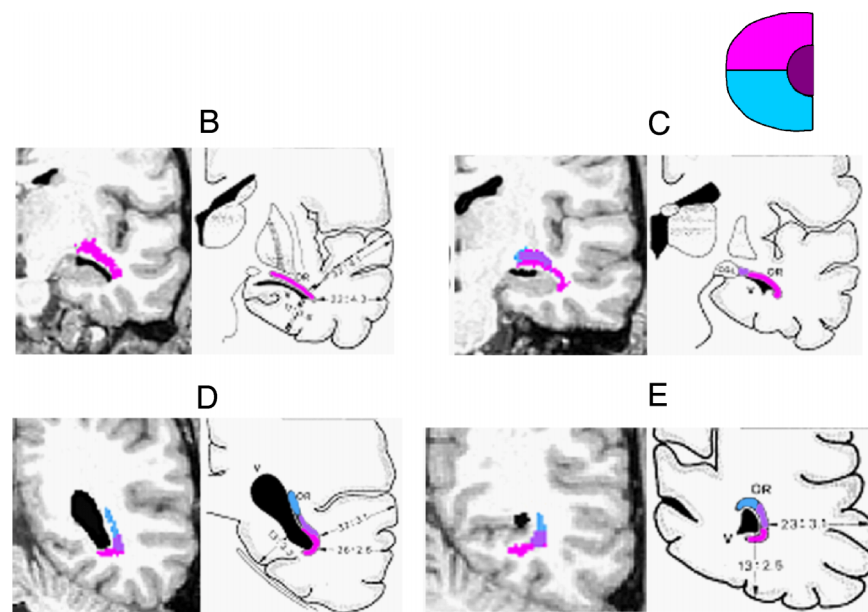


Figure 5. Coronal sections showing the position of the direct, central, and Meyer's loop bundles within the OR. Each panel compares an MR image and estimated fibers (left) with illustrations from a dissection study (Ebeling & Reulen, 1988) (right). The positions of the OR bundles are shown by the color overlays, and the expected visual information carried by these bundles is indicated by the inset (upper right). The locations of the coronal slices (B, C, D, and E) are shown in Figure 3. Subject S1.

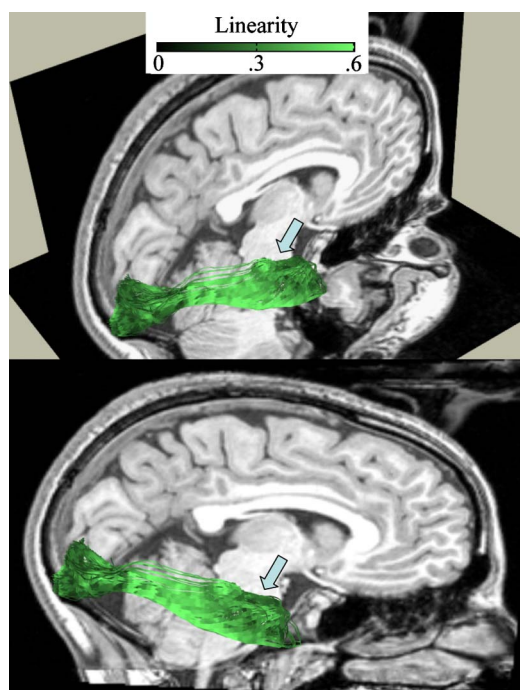


Figure 6. Linearity index along the OR. The linearity index is sampled at 1-millimeter arc length. The linearity index value is shown by the inset. The T1-weighted background image is a sagittal right hemisphere slice, near the bottom of the calcarine sulcus. The two images show the same data from different viewpoints. Subject S2.

right OR diffusivities (Figure 7). The radial diffusivities are systematically higher in the right compared to the left hemisphere.

Discussion

A series of neurological reports discuss the disruption of the visual field following resection of the anterior temporal lobe. Hughes et al. (1999) observed that nearly every patient they measured showed a visual field loss when measured using automated static perimetry (Humphrey visual fields). They note that these patients were not aware of this loss; it was only revealed by formal testing. Roughly half of the patients lost visual field sensitivity within 9 deg of the fovea, and a quarter of the patients lost visual field within 3 deg of the fovea.

Krolak-Salmon et al. (2000) report that 15 of 18 patients presented with a post-operative visual field loss. They report two cases in which the resection was limited to 20 mm from the temporal pole but still produced a partial quadrantanopia.

In both Hughes et al. (1999) and Krolak-Salmon et al. (2000), the post-operative visual field loss was in the upper visual field, consistent with our understanding of the

information carried on the anterior portion of Meyer's loop. Hence, these reports suggest that the resection specifically damages the anterior portion of Meyer's loop, which typically is located near the temporal horn.

Population statistics from anatomical measurements are used to guide tissue resection (Choi et al., 2006; Ebeling & Reulen, 1988; Peltier et al., 2006; Rubino et al., 2005; Sincoff et al., 2004; Yasargil et al., 2004). But there is considerable individual variability in the precise position of the anterior portion of Meyer's loop, as reported in (Ebeling & Reulen, 1988) and in our results here. Hence, it is probably not practical to identify a single fixed position as a safe limit for resection. The individual variability makes it greatly preferable to identify the location of Meyer's loop in each patient.

Related literature

We compare various estimates of the position of Meyer's loop in Table 2. The table shows the position of the anterior portion of Meyer's loop (MLa) with respect to several anatomical landmarks (see Figure 3).

The gold standard for pre-operative detection of the course of the OR is based on the gross dissection technique on frozen, formalin fixed tissue (Klingler method) (Ebeling & Reulen, 1988). These estimates, shown in the first data column, agree very closely with the ConTrack estimates (second data column). The Ebeling and Reulen (1988) study is also used as the gold standard for OR location measurements in two previous

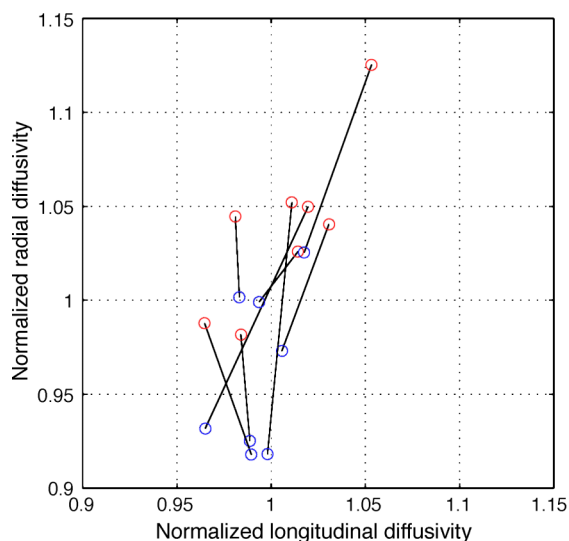


Figure 7. Scatter plot of radial and longitudinal diffusivity comparing left (blue) and right (red) hemispheres. Points from individual subjects are connected by a line. The radial diffusivity is approximately 7% higher, on average, in the right hemisphere. Only voxels with a linearity index above 0.3 are included in the calculation. The axes are normalized to the mean longitudinal ($1.57 \mu\text{m}^2/\text{msec}$) or radial ($0.45 \mu\text{m}^2/\text{msec}$) diffusivity.

t2.1	Measurement	Dissection (Ebeling & Reulen, 1988), $X \pm SD$ min–max (mm)	ConTrack (Sherbondy et al., 2008), $X \pm SD$ min–max (mm)	STT (Yamamoto et al., 2005), $X \pm SD$ min–max (mm)	STT (Nilsson et al., 2007), $X \pm SD$ min–max (mm)
t2.2	MLa–TP	27 ± 3.5	28 ± 3.0	37 ± 2.5	44 ± 4.9
t2.3	(distance)	22 – 37	24 – 34	33 – 40	34 – 51
t2.4	MLa–OP	98 ± 6.2	96 ± 5.5	82 ± 3.0	NA
t2.5	(distance)	85 – 108	89 – 108	77 – 85	
t2.6	MLa–TH	5 ± 3.2	3 ± 2.6	-4 ± 0.2	-15 ± 4
t2.7	(position)	–5 to 10	–1 to 8	–4.3 to –3.7	–21 to –8

Table 2. Distance between the anterior position of Meyer’s loop (MLa) and other anatomical landmarks. The rows indicate the distance between the MLa and (1) the temporal pole (TP), (2) the occipital pole (OP), and (3) the temporal horn (TH); anterior is positive relative to the TH. The four data columns are estimates from Ebeling and Reulen (1988), ConTrack, Yamamoto et al. (2005), and Nilsson et al. (2007). Measurements by Ebeling and Reulen and ConTrack (columns 1 and 2) are in good agreement. The mean position of the MLa, as measured by Yamamoto et al. and Nilsson et al. (columns 3 and 4), differ from Ebeling and Reulen by more than 1 cm, posterior.

DTI-FT methods (Nilsson et al., 2007; Yamamoto et al., 2005) and the data have been confirmed by additional dissection (Choi et al., 2006; Peltier et al., 2006; Rubino et al., 2005) and clinical studies (Hughes et al., 1999; Krolak-Salmon et al., 2000).

Two previous measurements of the OR position based on STT methods are shown in the third and fourth data columns (Nilsson et al., 2007; Yamamoto et al., 2005). These authors estimate the mean anterior position of Meyer’s loop to be at least 1 cm posterior to estimates from dissection studies (Ebeling & Reulen, 1988).

For example, Nilsson et al. (2007) find the temporal horn 1.5 cm anterior to Meyer’s loop. They suggest that the discrepancy may be due to mis-identification of the fibers during dissection or errors in the dissection estimates of absolute distances. Distance errors are not an adequate explanation because the anatomical descriptions also include ordering information. For example, Sincoff et al. (2004) writes: “The anterior tip of the temporal horn was covered by the anterior optic radiation along its lateral half (abstract).” Choi et al. (2006) writes: “In all of our specimens, the anterior edge of the Meyer’s loop reached the tip of the temporal horn (p. 232; see also Figure 3 in that article).” Forced to choose between DFT estimates and anatomical dissection at this point in time, we think anatomists should have priority.

The high false-negative (miss) rate of the STT algorithms has been reported in the literature, and there has been much progress on new algorithms designed to address this issue. Specifically, probabilistic methods have been developed to address the uncertainty within the diffusion data and locate valid pathways previously hidden to STT (Anwander, Tittgemeyer, von Cramon, Friederici, & Knosche, 2006; Behrens, Woolrich, et al., 2003; Bjornemo, Brun, Kikinis, & Westin, 2002; Friman & Westin, 2005; Hagmann et al., 2003; Hosey, Williams, & Ansoorge, 2005; Lazar & Alexander, 2002; Parker, Haroon, & Wheeler-Kingshott, 2003; Perrin et al., 2005). As we have previously reported, many of these new techniques also fail to identify valid white matter path-

ways. Elsewhere, we specifically considered the problem these algorithms have with identifying the optic radiation and Meyer’s loop (Sherbondy et al., 2008).

Despite the known limits of STT algorithms, their computational simplicity and ease of interpretation are very attractive for clinical applications. Thus, several groups have applied STT to identify Meyer’s loop and predict the visual consequences of temporal lobe resections and disease (Kikuta et al., 2006; Okada et al., 2007; Yamamoto et al., 2007; Yamamoto et al., 2005). To identify Meyer’s loop with STT (e.g., FACT), investigators use the following approach. First, they use a brute force approach for identifying a large set of fibers within each hemisphere. The threshold for terminating a fiber path, in particular the threshold for the turn angle, is set to a liberal value. They then identify a series of regions of interest at the locations that are characteristic of the optic radiation, including the Meyer’s loop position and regions near the LGN and calcarine cortex. The fibers that fall within these regions, and not other identifiable regions, are the estimated OR fibers.

Okada et al. (2007) used this method to identify the OR in patients with arteriovenous malformations (AVMs). In a series of patients, they observed a correlation between visual field loss and the ability to identify intact optic radiation fibers. Using a similar approach, Kikuta et al. (2006) report a similar correlation between visual performance and the ability to track OR fibers. Neither group assessed whether the position of the estimated OR matched controls because neither group studied normal controls. Finally, even without tractography, Taoka et al. (2005) showed that basic diffusion properties, such as fractional anisotropy within manually segmented optic radiation, was a useful predictor of visual performance.

These studies illustrate that diffusion-weighted imaging and tractography contains a great deal of useful information about the optic radiation and that these measures relate to visual performance. The Yamamoto et al. (2005) study shows that the STT approach to identifying these pathways gives a first approximation but does not match

534 the gold standard identified in dissection studies (Ebeling
535 & Reulen, 1988).

536 The ConTrack method improves the estimation preci-
537 sion for the optic radiation considerably. Specifically,
538 ConTrack estimates reduce the error from a centimeter or
539 more in STT methods to within the error rate of the
540 dissection method (millimeters). This increased precision
541 should provide us with better guidance during surgical
542 procedures, and it should also enable visual neuroscient-
543 ists to measure the position and properties of the optic
544 radiation accurately.
545

546 Acknowledgments

548 The authors thank Dr. P. Basser for discussion of the
549 ConTrack algorithm, Dr. N. Imbar for help in optic
550 radiation analysis, and Dr. R. Bammer for data acquisition
551 assistance. Supported by NIH EY015000.

AQ22 Commercial relationships: none.

553 Corresponding author:

554 Email:

555 Address:

556 References

558 Andrews, T. J., Halpern, S. D., & Purves, D. (1997).
559 Correlated size variations in human visual cortex,
560 lateral geniculate nucleus, and optic tract. *Journal of*
561 *Neuroscience*, 17, 2859–2868.

562 Anwander, A., Tittgemeyer, M., von Cramon, D. Y.,
563 Friederici, A. D., & Knosche, T. R. (2006). Con-
564 nectivity-based parcellation of Broca's area. *Cerebral*
AQ45 *Cortex*.

566 Basser, P. J., Pajevic, S., Pierpaoli, C., Duda, J., &
567 Aldroubi, A. (2000). In vivo fiber tractography using
568 DT-MRI data. *Magnetic Resonance in Medicine*, 44,
569 625–632.

570 Behrens, T. E., Johansen-Berg, H., Woolrich, M. W.,
571 Smith, S. M., Wheeler-Kingshott, C. A., Boulby, P. A.,
572 et al. (2003). Non-invasive mapping of connections
573 between human thalamus and cortex using diffusion
574 imaging. *Nature Neuroscience*, 6, 750–757.

575 Behrens, T. E., Woolrich, M. W., Jenkinson, M., Johansen-
576 Berg, H., Nunes, R. G., Clare, S., et al. (2003).
577 Characterization and propagation of uncertainty in
578 diffusion-weighted MR imaging. *Magnetic Resonance*
579 *in Medicine*, 50, 1077–1088.

580 Bjornemo, M., Brun, A., Kikinis, R., & Westin, C. (2002).
581 *Regularized stochastic white matter tractography*
582 *using diffusion tensor MRI*. Paper presented at the
583 MICCAI.

Catani, M., Jones, D. K., Donato, R., & Ffytche, D. H. 584
(2003). Occipito-temporal connections in the human 585
brain. *Brain*, 126, 2093–2107. 586

Choi, C., Rubino, P. A., Fernandez-Miranda, J. C., Abe, H., 588
& Rhoton, A. L., Jr. (2006). Meyer's loop and the optic 589
radiations in the transylvian approach to the medi- 590
obasal temporal lobe. *Neurosurgery*, 59, 235–226. 591

Ciccarelli, O., Toosy, A. T., Hickman, S. J., Parker, G. J., 593
Wheeler-Kingshott, C. A., Miller, D. H., et al. (2005). 594
Optic radiation changes after optic neuritis detected 595
by tractography-based group mapping. *Human Brain* 596
Mapping, 25, 308–316. 597

Conturo, T. E., Lori, N. F., Cull, T. S., Akbudak, E., 599
Snyder, A. Z., Shimony, J. S., et al. (1999). Tracking 600
neuronal fiber pathways in the living human brain. 601
Proceedings of the National Academy of Sciences of 602
the United States of America, 96, 10422–10427. 603

Ebeling, U., & Reulen, H. J. (1988). Neurosurgical 605
topography of the optic radiation in the temporal 606
lobe. *Acta Neurochirurgica*, 92, 29–36. 607

Friman, O., & Westin, C. F. (2005). Uncertainty in white 608
matter fiber tractography. In *Proceedings of the* 609
Medical Image Computing and Computer-Assisted 610
Intervention, 8, 107–114. 611

Friston, K., & Ashburner, J. (2004). *Statistical parametric* 612
mapping. Retrieved from [http://www.fil.ion.ucl.ac.uk/](http://www.fil.ion.ucl.ac.uk/spm/software/spm2/) 613
[spm/software/spm2/](http://www.fil.ion.ucl.ac.uk/spm/software/spm2/). 614

Hagmann, P., Thiran, J. P., Jonasson, L., Vandergheynst, P., 615
Clarke, S., Maeder, P., et al. (2003). DTI mapping of 616
human brain connectivity: Statistical fibre tracking and 617
virtual dissection. *Neuroimage*, 19, 545–554. 618

Hosey, T., Williams, G., & Ansorge, R. (2005). Inference 619
of multiple fiber orientations in high angular reso- 620
lution diffusion imaging. *Magnetic Resonance in* 621
Medicine, 54, 1480–1489. 622

Hughes, T. S., Abou-Khalil, B., Lavin, P. J., Fakhoury, T., 623
Blumenkopf, B., & Donahue, S. P. (1999). Visual field 624
defects after temporal lobe resection: A prospective 625
quantitative analysis. *Neurology*, 53, 167–172. 626

Jbabdi, S., Woolrich, M. W., Andersson, J. L., & Behrens, 627
T. E. (2007). A Bayesian framework for global 628
tractography. *Neuroimage*, 37, 116–129. 629

Jones, D. K. (2004). The effect of gradient sampling 630
schemes on measures derived from diffusion tensor 631
MRI: A Monte Carlo study. *Magnetic Resonance in* 632
Medicine, 51, 807–815. 633

Kikuta, K., Takagi, Y., Nozaki, K., Hanakawa, T., Okada, T., 634
Miki, Y., et al. (2006). Early experience with 3-T 635
magnetic resonance tractography in the surgery of 636
cerebral arteriovenous malformations in and around 637
the visual pathway. *Neurosurgery*, 58, 331–337. 638

Krolak-Salmon, P., Guenot, M., Tiliket, C., Isnard, J., 639
Sindou, M., Mauguiere, F., et al. (2000). Anatomy of 640

- 641 optic nerve radiations as assessed by static perimetry
642 and MRI after tailored temporal lobectomy. *British*
643 *Journal of Ophthalmology*, *84*, 884–889.
- 645 Lazar, M., & Alexander, A. L. (2002). *White matter*
646 *tractography using random vector (RAVE) perturba-*
647 *tion*. Paper presented at the Proceedings of ISMRM
648 Annual Meeting, Honolulu.
- 650 Leuret, F., & Gratiolet, L.-P. (1839). *Anatomie comparée*
651 *du Système Nerveux. Considéré dans ses rapports*
652 *avec l'Intelligence* (vol. II). Paris: J-B Baillière et fils.
- 654 Meyer, A. (1907). The connections of the occipital lobes
655 and the present status of the cerebral visual affections.
656 *Transactions Association of the American Physicians*,
657 *22*, 7–23.
- 659 Miller, N. R. (2005). Diffusion tensor imaging of the
660 visual sensory pathway: Are we there yet? *American*
661 *Journal of Ophthalmology*, *140*, 896–897.
- 663 Mori, S., Crain, B. J., Chacko, V. P., & van Zijl, P. C.
664 (1999). Three-dimensional tracking of axonal projec-
665 tions in the brain by magnetic resonance imaging.
666 *Annals of Neurology*, *45*, 265–269.
- 668 Nilsson, D., Starck, G., Ljungberg, M., Ribbelin, S., Jonsson,
669 L., Malmgren, K., et al. (2007). Intersubject variability
670 in the anterior extent of the optic radiation assessed by
671 tractography. *Epilepsy Research*, *77*, 11–16.
- 673 Okada, T., Miki, Y., Kikuta, K., Mikuni, N., Urayama, S.,
674 Fushimi, Y., et al. (2007). Diffusion tensor fiber
675 tractography for arteriovenous malformations: Quan-
676 titative analyses to evaluate the corticospinal tract and
677 optic radiation. *American Journal of Neuroradiology*,
678 *28*, 1107–1113.
- 680 Parker, G. J., Haroon, H. A., & Wheeler-Kingshott, C. A.
681 (2003). A framework for a streamline-based proba-
682 bilistic index of connectivity (PICO) using a structural
683 interpretation of MRI diffusion measurements. *Jour-*
684 *nal of Magnetic Resonance Imaging*, *18*, 242–254.
- 686 Peled, S., Gudbjartsson, H., Westin, C. F., Kikinis, R., &
687 Jolesz, F. A. (1998). Magnetic resonance imaging
688 shows orientation and asymmetry of white matter
689 fiber tracts. *Brain Research*, *780*, 27–33.
- 691 Peltier, J., Travers, N., Destrieux, C., & Velut, S. (2006).
692 Optic radiations: A microsurgical anatomical study.
693 *Journal of Neurosurgery*, *105*, 294–300.
- 695 Perrin, M., Poupon, C., Cointepas, Y., Rieul, B., Golestani,
696 N., Pallier, C., et al. (2005, July). Fiber tracking in
697 q-ball fields using regularized particle trajectories. In
698 *Proceedings of the 19th International Conference on*
699 *Information Processing in Medical Imaging (IPMI*
700 *'05)*, Glenwood Springs, CO (pp. 52–63).
- 701 Powell, H. W., Parker, G. J., Alexander, D. C., Symms,
702 M. R., Boulby, P. A., Wheeler-Kingshott, C. A., et al.
703 (2005). MR tractography predicts visual field defects
704 following temporal lobe resection. *Neurology*, *65*,
705 596–599.
- Rohde, G. K., Barnett, A. S., Basser, P. J., Marenco, S., 706
& Pierpaoli, C. (2004). Comprehensive approach for 707
correction of motion and distortion in diffusion- 708
weighted MRI. *Magnetic Resonance in Medicine*, *51*, 709
103–114. 710
- Rohde, G. K., Barnett, A. S., Basser, P. J., & Pierpaoli, C. 712
(2005). Estimating intensity variance due to noise in 713
registered images: Applications to diffusion tensor 714
MRI. *Neuroimage*, *26*, 673–684. 715
- Rubino, P. A., Rhoton, A. L., Jr., Tong, X., & Oliveira, E. 717
(2005). Three-dimensional relationships of the optic 718
radiation. *Neurosurgery*, *57*, 219–227; discussion 719
219–227. 720
- Schmahmann, J. D., & Pandya, D. N. (2006). *Fiber*
721 *pathways of the brain*. New York: Oxford University
722 Press. 723
724
- Sherbondy, A., Akers, D., Mackenzie, R., Dougherty, R., 726
& Wandell, B. (2005). Exploring connectivity of the 727
brain's white matter with dynamic queries. *IEEE*
728 *Transactions on Visualization and Computer*
729 *Graphics*, *11*, 419–430. 730
- Sherbondy, A., Dougherty, R., Ben-Shachar, M., Napel, S., 732
& Wandell, B. (2008). ConTrack: Finding the most 733
likely pathways between brain regions using diffusion 734
tractography. *Journal of Vision*, *8(9):15*, 1–16, [http://](http://journalofvision.org/8/9/15/)
735 journalofvision.org/8/9/15/, doi:10.1167/8.9.15. 736
- Sincoff, E. H., Tan, Y., & Abdulrauf, S. I. (2004). White 738
matter fiber dissection of the optic radiations of the 739
temporal lobe and implications for surgical 740
approaches to the temporal horn. *Journal of Neuro-*
741 *surgery*, *101*, 739–746. 742
- Taoka, T., Sakamoto, M., Iwasaki, S., Nakagawa, H., 744
Fukusumi, A., Hirohashi, S., et al. (2005). Diffusion 745
tensor imaging in cases with visual field defect after 746
anterior temporal lobectomy. *American Journal of*
747 *Neuroradiology*, *26*, 797–803. 748
- Yamamoto, A., Miki, Y., Urayama, S., Fushimi, Y., 749
Okada, T., Hanakawa, T., et al. (2007). Diffusion 750
tensor fiber tractography of the optic radiation: 751
Analysis with 6-, 12-, 40-, and 81-directional 752
motion-probing gradients, a preliminary study. *Amer-*
753 *ican Journal of Neuroradiology*, *28*, 92–96. 754
- Yamamoto, T., Yamada, K., Nishimura, T., & Kinoshita, S. 755
(2005). Tractography to depict three layers of visual 756
field trajectories to the calcarine gyri. *American*
757 *Journal of Neuroradiology*, *140*, 781–785. 758
- Yasargil, M. G., Ture, U., & Yasargil, D. C. (2004). 759
Impact of temporal lobe surgery. *Journal of Neuro-*
760 *surgery*, *101*, 725–738. 761
- Yushkevich, P. A., Piven, J., Hazlett, H. C., Smith, R. G., 762
Ho, S., Gee, J. C., et al. (2006). User-guided 3D 763
active contour segmentation of anatomical structures: 764
Significantly improved efficiency and reliability. 765
Neuroimage, *31*, 1116–1128. 766

AUTHOR QUERIES

AUTHOR PLEASE ANSWER ALL QUERIES

AQ1: Please provide e-mail and Web address, if any.

AQ2: Please provide data for author's correspondence.

AQ3: Please provide [PubMed] and/or [Article] links for the references.

AQ4: Please provide the volume number and the page range.

END OF AUTHOR QUERIES